A thermally actuated biocompatible flexible micropump for surface adaptable mounting

Victor Bradley Bednar[1] · Kenichi Takahata[1]

Abstract

Pulsed thermal energy causes piecewise actuation of a nitinol cantilever providing the mechanical force required to evacuate a chamber constructed of parylene C. This proof-of-principle micropump demonstrates an alternative to typical evacuation and rectification methods utilized in most micropumps. The chamber and normally closed channels that serve as valves are all of parylene C construction, leading to the flexibility of the device. The nitinol cantilever functions as an actuator capable of yielding successive partial chamber evacuations until achieving complete evacuation. Piecewise shape recovery of the actuator was made viable by implementing a Peltier device, providing the means for supplying responsive and controlled thermal energy. Experiments delivered measurements of consecutive advancement of shape recovery using a laser displacement sensor while monitoring the temperature with fiber-optic sensors. The release of a saturated lithium chloride solution from the pump was monitored by observing conductivity changes in the experimental area. Theoretically predicting a release amount used calculations for the expected recovery of the actuator based on displacement characterization via a logistic curve fit against actuator temperature data. The measured release amounts correlated well with the theoretically predicted values made using the temperature values obtained near the device during the release. These works provide novel approaches to micropump fabrication and implementation and new strategies for predicting the recovery of shape memory alloys. The micropump concepts are viable in many fields, such as biomedical applications: in vivo drug delivery, organ-on-chip, and lab-on-chip devices, to name a few. Likewise, a simple prediction for nitinol recovery has vast potential.

1 Introduction

Micropumps provide the driving force for fluid motion, making them an integral component in microfluidics. Numerous applications have seen various micropump designs developed over the years (Mohith et al. 2019). Numerous review papers provide a dichotomy on the various types of micropumps. The first division is usually a separation between mechanical and non-mechanical driving forces (Barua et al. 2021; Chappel and Dumont-Fillon 2021; Wang and Fu 2018;

✉ Victor Bradley Bednar
victor@ece.ubc.ca

Kenichi Takahata
takahata@ece.ubc.ca

1 Department of Electrical and Computer Engineering, University of British Columbia, Vancouver, BC V6T1Z4, Canada

Mohith et al. 2019). For many microfluidic devices, controlling fluids can be broken down into three categories when considering only mechanical interactions. There are elements for controlling the direction and quantity of flow, typically done with valves. In recent years, nozzles and diffusers have been proving capable of manipulating the direction and amount of fluid flow (Mohith et al. 2019). Holding areas, places to contain fluid, will be referred to as chambers in this document. Channels direct the flow of fluids using obstructions along a path. A unique aspect of micropumps is that many designs contain one or more of all three components, chambers, valves, and channels.

Though non-mechanical methods can control fluid motion, the implementation of such forces narrows the applications for a device. For example, a device using electromagnetic fields to manipulate a charged fluid can only operate when working with a charged fluid. This implication only runs in one direction. In juxtaposition, a device made

to drive the motion of an uncharged fluid can still function when working with a charged fluid. For this reason, the driving force used to demonstrate the operational capabilities of our pump will come from a mechanical method.

Considering the mechanical actuation methods available, shape-memory materials (SMMs) made with nitinol are of particular interest due to their inherent biocompatibility.

In these works, many focused improvements target areas with room for growth in micropump research. The overall design, volume efficiency, fabrication simplicity, and adaptability are improvement objectives. As many micropumps have package sizes ranging from hundreds to thousands of cubic millimeters (Forouzandeh et al. 2021; Mohith et al. 2019), going smaller while maintaining a reasonable percentage of the package as containment volume for the working fluid is of particular interest.

One novel overall design improvement is achieving multiple evacuations from the chamber without needing to rectify the chamber area. Typical micropump designs include a cyclic motion that evacuates fluid from the pump chamber and then requires refilling from a reservoir (Wang and Fu 2018; Barua et al. 2021; Chappel and Dumont-Fillon 2021; Forouzandeh et al. 2021; Mohith et al. 2019). While the pump design presented here is adaptable for such an operation, the idea is to free the need for a separate reservoir chamber. Doing so also removes the need for reservoir connection and flow control; videlicet, both a channel and a valve between the chamber and reservoir are no longer needed. Other works have similarly moved away from typical designs for similar pursuits (Tang et al. 2020). Removing typically required components saves fabrication steps and design space; accordingly, the conditions of the second and third objectives are satisfied.

Another novel overall design improvement comes from using normally closed flexible channels as valves. The inspiration for this improvement comes from external pressure used as the force for closing valves (Lee et al. 2018) combined with the flow profile through flexible channels (Christov et al. 2018; Mehboudi and Yeom 2019). This design removes the fabrication steps and space needed when employing typical valve designs. Again, this satisfies the conditions of the second and third objectives. This feature should also make using arrays of various multi-pump configurations simple. Multi-chamber pump designs benefit from enhanced performance over directly comparable single chamber devices (Mohith et al. 2019).

Finally, adaptability is addressed by making the chamber and closed channels out of parylene C. That creates a flexible device capable of performing in a wide array of environments due to the chemically resistant nature of parylene C. Flexibility in and of itself is a design improvement that many devices are taking advantage of in recent years. (Fallahi et al. 2019). The closed channels can

connect to various microfluidic systems; however, the targeted application to be established in future publications will be for a drug delivery device. Though parylene C has been used previously for a flexible substrate (Chen et al. 2007), to our knowledge, this is the first instance of and all parylene design.

In Sect. 2, the concepts and working principles (Sects. 2.1 and 2.2) for the prototype pump are outlined. The conductivity and temperature data collection setup (Sect. 2.3) along with relevant data manipulation (Sect. 2.4) and material selection (Sect. 2.5) for sensor detection are also explained. Then, the fabrication and experimental methods are described in Sect. 3. Section 3 includes the actuator's fabrication (Sect. 3.1), the pump chamber's and flexible closed channel's fabrication (Sect. 3.2), various characterizations (Sects. 3.3, 3.4 and 3.6), and the experimental setup used for temperature-controlled release measurements (Sect. 3.5). The results of the temperature-controlled release are presented and analyzed in Sect. 4. Concluding remarks are in Sect. 5.

2 Theory and concepts

One of the major drawbacks often found with SMMs is the time to restore and then deform the actuator for a cyclic pumping action. These works deviate from that approach and instead control the fluid delivery by incremental restoration of a deformed actuator. The concept for this is explained in Sect. 2.1.

Another novel concept in this pump is the choice to use the elastic properties of parylene C to make a normally closed channel acting as a valve. The working principle for valve operation is presented in Sect. 2.2.

When considering measuring the release of nanoliter volumes from a device, options are limited, and if real-time data collection is desirable, these limitations increase. One solution for data collection of small fluid volumes released into another fluid is monitoring optical transmission data in real time.

Optical measurements offer high temporal and spatial precision, allowing fast readings (milliseconds) on small sample sizes (microliters). The trade-offs are high operational costs and susceptibility to ambient noise.

A much more cost-effective way to measure this information is with electrical conductivity measurements in a fluid (Bednar and Takahata 2021). The setup for measuring conductivity and temperature is provided in Sect. 2.3. There are many factors to consider when using conductivity measurements to track fluid release. Select relevant variables will be presented in Sects. 2.4 and 2.5.
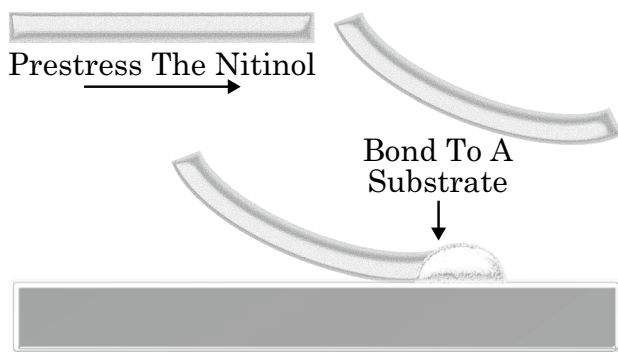
Fig. 1 An illustration of the nitinol actuator preparation via prestressing and bonding

2.1 Nitinol actuator working principle

Nitinol characterization has shown that shape recovery has loss through cycling. This has been described as a retention in some of the martensite phase after the transition to the austenite phase (Miller and Lagoudas 2000). Though there is some loss in the amount of recovery, this diminishes with each cycle, seemingly approaching a saturation limit (Kumar and Lagoudas 2008). In order to account for this eventually unrecoverable plastic deformation, prestressing the actuator prior to bonding is our proposed solution. As seen in Fig. 1, by prestressing and then bonding the actuator, the original shape will not be achieved even when contact with the substrate is complete. This serves multiple purposes. As mentioned, it can allow gap free closure, applying pressure even to the point of contact with the substrate, despite some small loss in available shape recovery. It can also be used for flexible substrate mounting, allowing recovery toward an undetermined curve. Both of these functions are similar to observed traits in constrained recovery for SMM fasteners and couplings (Alaneme and Okotete 2016).

Another characteristic of SMMs is that they do not instantaneously recover shape at a specific temperature, but rather, they recover toward their original shape over a range of temperatures. While this transient response is often characterized during a fixed temperature exposure, and many SMMs are modified with the intent of changing the recovery time (Wu et al. 2013; Ni et al. 2023), few examples exist to exploit this nature. Instead many actuators focus on recovery to an endpoint or cyclic behaviors (Renata et al. 2017). Partial recovery is viewed as a challenge, because of the difficulties in modeling and controlling piecewise actuation (Abdullah et al. 2021). Yet, select studies have shown promising results using wires or fibers for precise force control of the tension in nitinol or composite materials (Babu and Mathew 2014; Yamashita and Shimamoto 2005). In these works, we demonstrate controllable, piecewise actuation through pulsed energy cycles. Reshaping the actuator after prestressing allows for better space efficiency when used with the pump chamber. Each heating cycle achieves a slightly higher temperature than the previous, leading to incremental thermal recovery as depicted in Fig. 2.

## 2.2 Normally closed valve working principle

Normally closed valves remain closed in the absence of a stimulus or mechanism that causes them to open. In order to maintain this closure, the elasticity of parylene C has been exploited. Due to the alignment of the channels connecting to the chamber, bonding of the pump to a substrate under pressure causes the stretching of the top layer of parylene closing over the channel. This tension holds the channel closed under normal conditions (Fig. 3a). As pressure is applied to the chamber, the fluid forces the deformation of the channel due to its elastic structure and sufficient force causes the channel to open (Fig. 3b). Once the externally applied pressure is released, the channel returns to a closed state due to tension in the parylene C top layer. This repeatable cycle is the basis for progressively evacuating the chamber through a series of partial releases, alternating between the closed and open channel states seen in Fig. 3.

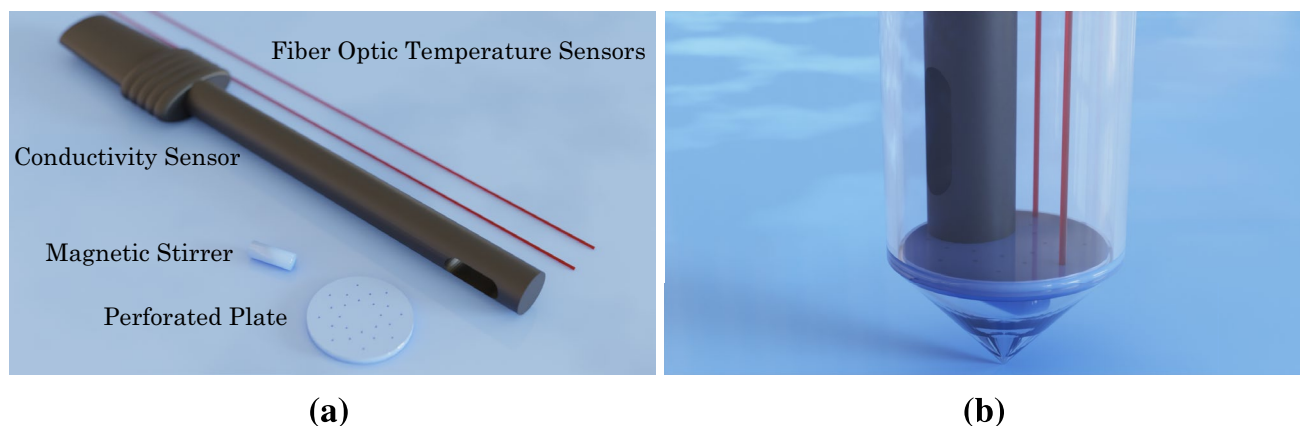## 2.3 Conductivity and temperature data collection setup

The data collection setup for conductivity and temperature (Fig. 4) was as follows: a conductivity probe (GDX-CON, Vernier, OR, USA), set to collect at one-second intervals from the provided software (Graphical Analysis 4, Vernier, OR, USA) on a computer connected via USB, was held by its electrode support (ESUP, Vernier, OR, USA) mounted to a lab stand support. Below the electrode support, a three-finger clamp held a centrifuge tube with 15 mL of deionized (DI) water to the same stand. A perforated plastic plate kept a stirring magnet in the bottom of the centrifuge tube. That separated the bottom from the experimental area above,
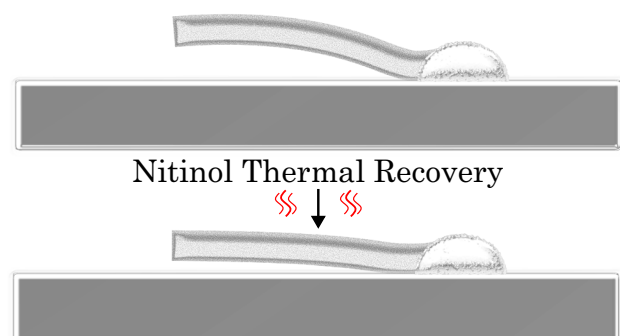
Fig. 2 An illustration of a reshaped nitinol actuator undergoing partial actuation via thermal stimulation
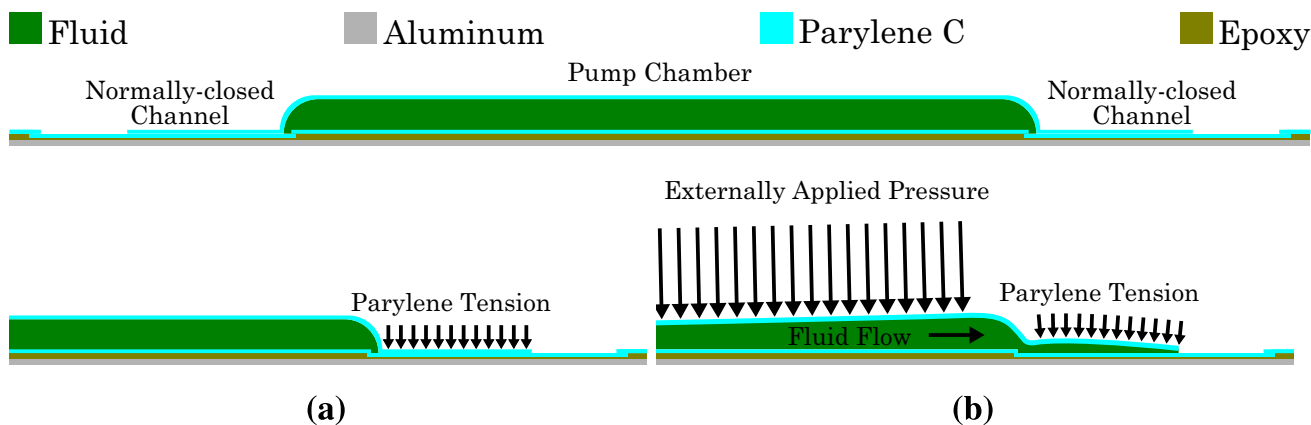
Fig. 3 A side view of the normally closed valve operation, **a** closed from tension induced during the bonding process, and **b** open with a sufficient externally supplied stimulus

Fig. 4 A to-scale, 3D computer-generated image of **a** the tools used for collecting conductivity and temperature data presented as simplified objects organized for viewing with labels alongside **b** a depiction of how they fit into a centrifuge tube

where the conductivity sensor rested. Two fiber-optic temperature sensors (FOT-M, FISO Technologies, QC, CA), connected to the same computer via a fiber-optic signal conditioner (UMI 4, FISO Technologies, QC, CA) that was communicating to the computer using a USB connection, provided temperature readings at 1-s intervals from its software (FISO Commander, FISO Technologies, QC, CA).

Data alignment from the sensors was made possible by removing the sensors simultaneously from the water in the centrifuge tube and replacing them while data collection was running, causing a dip that could later be aligned.

2.4 Temperature compensation for conductivity readings

In general, the conductivity of a solution increases with temperature. This increase in conductivity with temperature is reasonably linear for a set concentration over a limited temperature range; however, the slope is variable over different concentrations. Also, the rate of increase changes depending on the electrolyte in the solution. Other parameters, such as viscosity, affect the conductivity. The idea here is to observe the release of a set solution from a pump. As such, a single percentage value correction will adjust all conductivity readouts.

The conductivity probe suppliers (mentioned in Sect. 2.3) provided their formula for temperature compensation, labeled with 2% TC. This equation provides a linear adjustment to the conductivity readings as if measured at room temperature (25 °C).

$$C_{TC} = \frac{C}{1 - p(25 - T)} \tag{1}$$

In eq. (1), temperature compensated conductivity, C_{TC}, is equivalent to the measured conductivity, C, divided by unity minus the percent correction difference from room temperature. The percent correction difference is the product of p,

as a decimal value, with room temperature (25 °C) minus solution temperature, T in °C.

As seen in Fig. 5, the adjusted conductivity reading stays relatively constant over the provided variations in temperature. The experiments in these works were conducted over a smaller subset temperature range within the values seen. Thus, this compensation should prove sufficient in removing conductivity variations caused by temperature changes. Another benefit is the clear indication of instrumental noise influence on conductivity readings. During the heating sections of the graph, the values are shifted, correlating with the hotplate being on.

The generation of the data for Fig. 5 was created by taking the experimental setup (described in Sect. 2.3) and placing it in a water bath heated in a beaker by a hotplate for the water temperature-increasing sections. Moving the centrifuge tube to an ice bath caused the temperature-decreasing intervals of the graph. After completing two heating and cooling cycles,

a couple of drops of saturated lithium chloride water were added, at ~ 2300 s, causing a rise in the conductivity. Following the addition of lithium chloride, three more heating and cooling cycles were completed.

Perceiving some previously mentioned correlations becomes easier when observing the same data from Fig. 5 plotted with temperature versus conductivity; therefore, a scatter plot of the temperature versus conductivity is graphed from the first 2300 and the last 2947 s, using the same data from Fig. 5. A linear correlation between the temperature and the conductivity is apparent in Fig. 6. Interference caused by the hotplate induces a conductivity reading shift that is detectable by the sets of parallel groupings of data at medium and low concentrations. As in Fig. 5,6, the difference between the two conductivity values at a given temperature is easier to discern at a medium concentration after adding lithium chloride. This is because the relationship between temperature and conductivity is nonlinear

Fig. 5 A graphical depiction of the difference between the direct readout from the conductivity sensor and the conductivity calculated with temperature compensation, as shown in Eq. 1
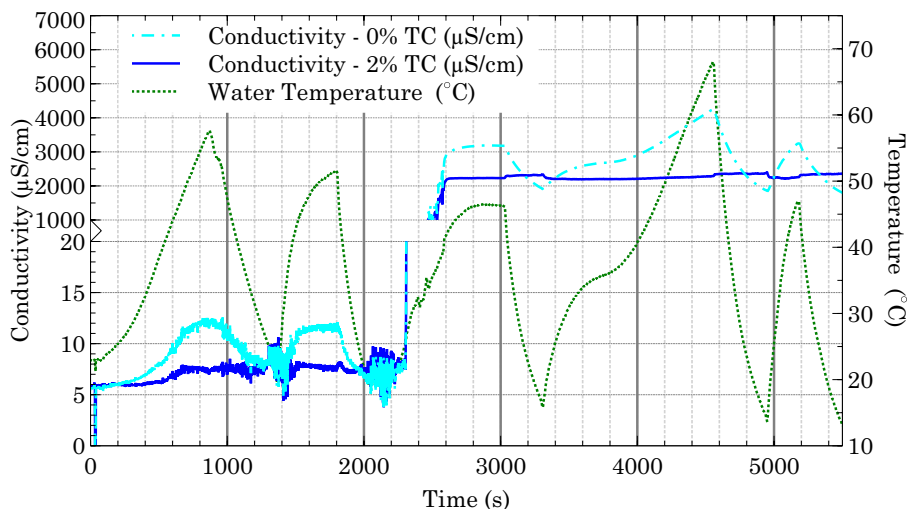
Fig. 6 A graphical illustration of the temperature from the first 2300 s and the last 2947 s of the experiment against the conductivity from the same data used for Fig. 5
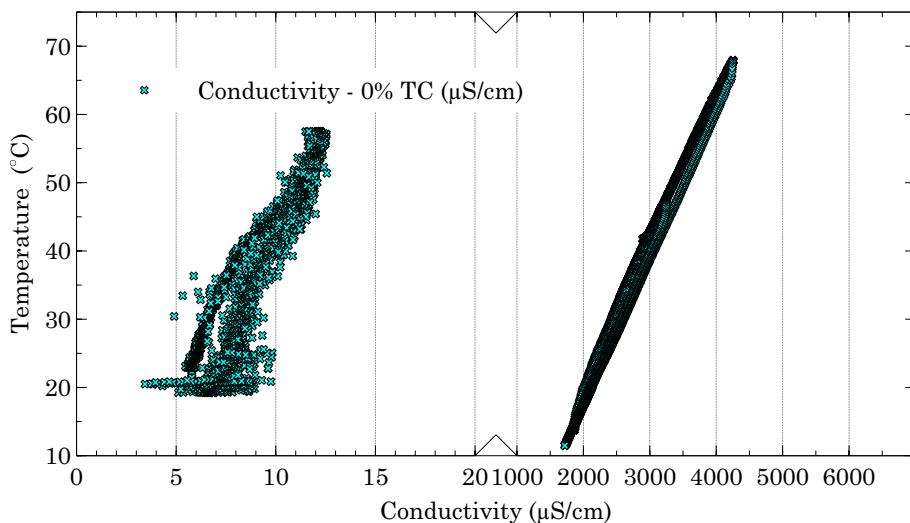
for ultra-pure water (less than 10 ppb). Thus, the DI water is starting to show some of this nonlinearity, especially at lower temperatures. It is also a much larger correlation slope for just the DI water. While most of the experiment will be conducted with enough ion concentration to ignore this information, it is important to note that low-concentration readings (near pure water) become less linear in correlation to temperature as do readings at low temperatures for those low concentrations. As a final observational note, the noise level from the sensor readings increases at low concentrations. This is partially due to the cell size (1 cm^3), which is most suitable for measurements in the range of 10–1000 µS/cm. As the readings are still accurate to ±1% for reading between 1 and 10,000 µS/cm it is not a cause for concern on the validity of the readings, only a trend worth noting.

2.5 Electrolyte selection

Electrolyte selection is possibly the most impactful decision when considering using conductivity to measure the release of one fluid volume into another. For these works, the selection criteria included safety, use of earth-conscientious materials, and cost-effectiveness.

Many variables exist when determining the effectiveness of an electrolyte. Thus, it becomes crucial to consider the experimental setup as a part of the selection process. For these works, a pump of approximately 100 nanoliters will release its contents into 15 mL of water. With five orders of magnitude difference between the volumes, it is no longer a problem of optimal concentration for conductivity. Instead, determining the highest concentration of charges containable in the 100 nanoliters is the problem.

A saturated solution should be in the pump to increase experimental sensitivity. Handling saturated acids, bases, or toxic chemicals poses high risks, avoidable when alternatives exist. Using water-soluble inorganic options avoids unnecessary solvent waste generation. Removing all those

options and considering earth abundance narrows the metal salt options down to the upper part of the periodic table. For the nonmetal component of the salt combinations, sticking with chlorine is a cost-effective option.

Among some remaining candidates, sorted based on the ionic radius, lithium has a much smaller radius than potassium (79 pm verses 138 pm respectively as proposed by (Mähler and Persson 2012)). Thus, comparing their chloride salts, lithium would polarize the molecule more. Polar solvents dissolve polar molecules. As water is polar, a higher solubility is both expected and observed for lithium chloride (a mole fraction of 0.2603 at 20.0 °C for lithium chloride (Cohen-Adad 1991) verses a mole fraction of 0.076 at 20.0 °C for potassium chloride (Cohen-Adad et al. 1991)). When comparing the change in conductivity observed after 10 drops of the saturated solution were added to DI water from a 20 gauge needle, as seen in Fig. 7b and 7a, lithium chloride rose slightly more than three times the amount from potassium chloride.

In order to validate this observation, the expected volume (*V*) from ten drops was calculated using Eq. 2 (values in Table 1). Then, using the mole fraction, the molarity of the saturated solutions was calculated (13.82 mol/L for lithium chloride and 4.004 mol/L for potassium chloride) in order to calculate the new molarity after addition into the 15 mL of water (0.1352 mol/L for lithium chloride and 0.03418 mol/L for potassium chloride). Finally, the new molarity values were converted to weight percent values (0.5732% for lithium chloride and 0.2548% for potassium chloride) to compare with expected values from both measured and calculated sources.

$$V = \frac{d\pi\gamma}{g\rho} \tag{2}$$

Averaging two separate values for each solution's conductivity measurements yielded 11,062.6 ± 61.6 µS/cm and
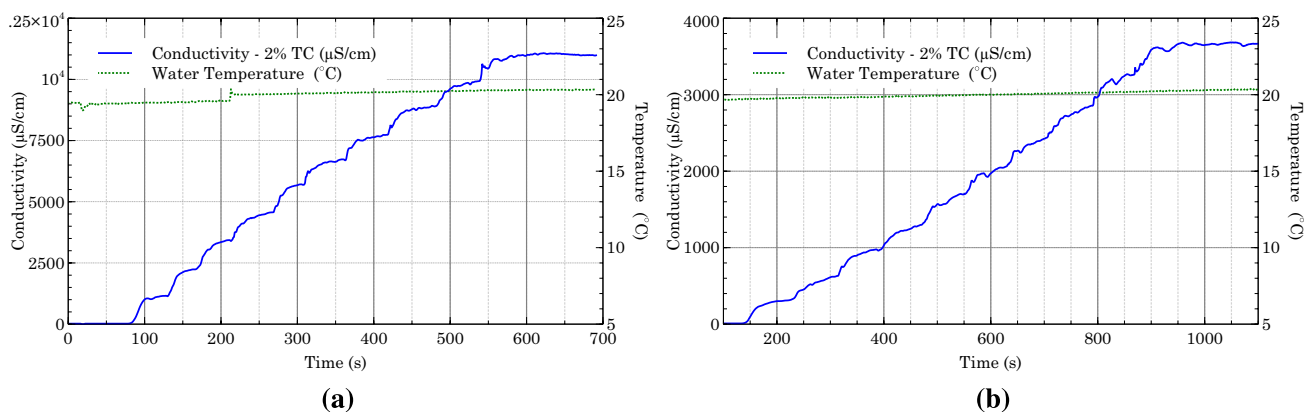
Fig. 7 A graphical comparison of releasing ten drops of saturated solution using **a** lithium chloride and **b** potassium chloride in water

Table 1 Volume calculation values for Eq. 2

Variable	Definition	Value	Units	Source
V_{LiCl}	10 drop volume, lithium chloride solution	148.3	μL	Calculated using Eq. 2
V_{KCl}	10 drop volume, potassium chloride solution	129.1	μL	Calculated using Eq. 2
d	Needle inner diameter	603	μm	
γ_{LiCl}	Surface tension, lithium chloride solution	99.24	$\frac{mN}{m}$	Calculated at 20 °C (Song et al. 2019)
γ_{KCl}	Surface tension, potassium chloride solution	78.58	$\frac{mN}{m}$	Measured at 23 °C (Ozdemir et al. 2009)
g	Gravity	9.80665	$\frac{m}{s^2}$	
ρ_{LiCl}	Density, lithium chloride solution	1.293	$\frac{g}{mL}$	Calculated at 20 °C (Cohen-Adad 1991)
ρ_{KCl}	Density, potassium chloride solution	1.1755	$\frac{g}{mL}$	Calculated at 20 °C (Cohen-Adad et al. 1991)

3652.6 ± 19.6 µS/cm for lithium chloride and potassium chloride, respectively. The table values from Emerson Process Management (2010) are 11,615 µS/cm 3700 µS/cm for lithium chloride and potassium chloride, respectively. The provided equation for potassium chloride yields a value of 3427.4 µS/cm (lithium chloride is outside the usable range (Emerson Process Management 2010)). Finally, fitting data from Rumble (2023) give 11,071.8 µS/cm 3900.5 µS/cm for lithium chloride and potassium chloride, respectively. Considering the range of accepted conductivity values, the results measured here fall within expectations. Thus, one can expect approximately three times the sensitivity when choosing lithium chloride over potassium chloride saturated solutions to be released into an environment many times the volume released.

While higher solubility allows for more sensitivity of volume release measurements, the observed dissolution rate is also much slower. A dilution of one-hundredth of the concentration from saturation makes a single drop contain an amount closer to the expected observable released from the pump. The diluted lithium chloride solution drops were dispensed at 700–800 s intervals, as seen in Fig. 8, and the conductivity readings plateau by waiting at least 200–300 s between releases. Thus, the sensitivity to measure small amounts of fluid releases comes with a loss in instantaneousness of the temporal observation for this decision.

3 Experimental methods

The pump creation was a three-step process. An electrochemical etch for creating an actuator, the fabrication of a pump chamber, and finally, integrating the pump chamber and actuator, as seen in Fig. 9. The actuator fabrication using electrochemical etching of nitinol is described in Sect. 3.1. Others have researched and characterized the electrochemical etching of nitinol (Mineta 2003; Mineta and Makino 2010). The pump chamber fabrication is described in Sect. 3.2. The in-plane dimensions of the ~ 100 nanoliter pump chamber are in the schematic diagram of Fig. 10.

After the nitinol actuator fabrication, confirmation of controlled piecewise actuation was necessary. Details for the setup and measurement of actuation are in Sect. 3.3.
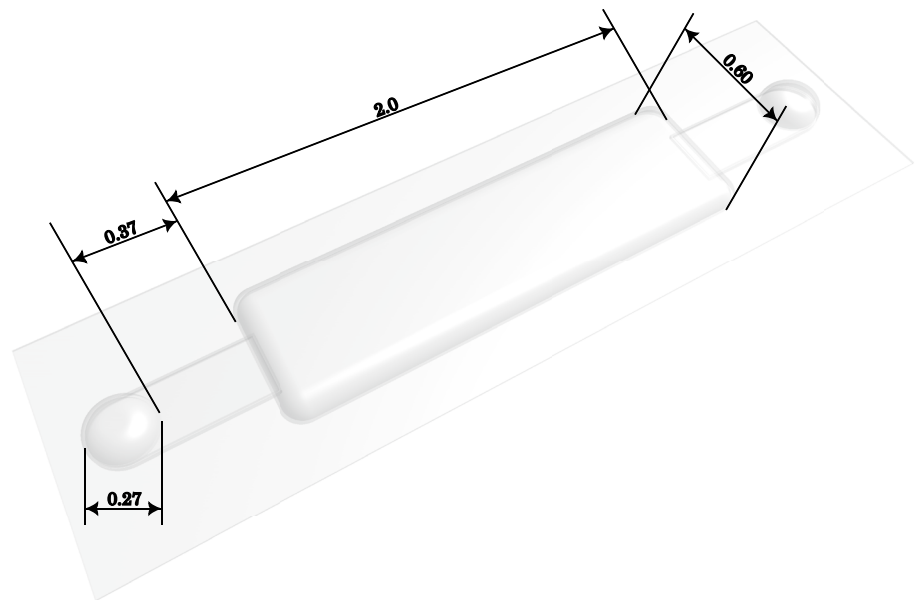
Fig. 8 A graph showing the release of five drops of lithium chloride solution, diluted at 1:100 from saturation in water
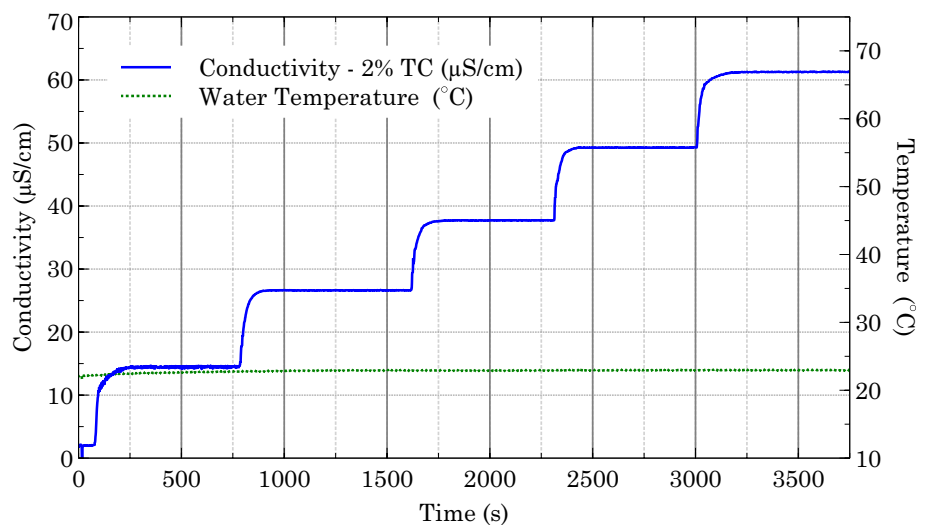
Fig. 9 A to-scale, 3D computer-generated image of the device as implemented in experiments with a bonded pump and a nitinol actuator
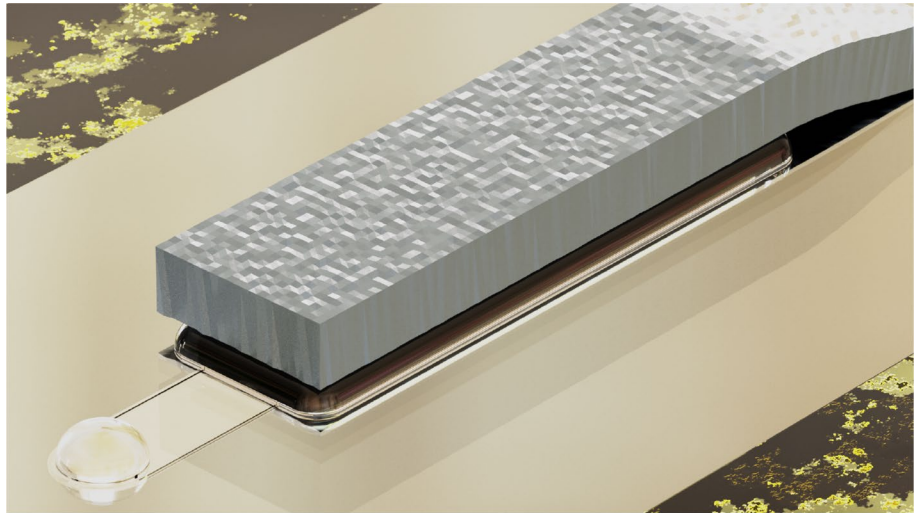
Fig. 10 A 3D computer-rendered image of the pump chamber, drawn to scale. The dimensions are in millimeters

After constructing the pump chamber, adhesion between parylene layers needed testing. Details on characterization to ensure integrity against leaking are in Sect. 3.4.

Building on the configuration in Sect. 2.3, for data collection to measure electrical conductivity and temperature, the setup and process for testing the pump releases are in Sect. 3.5. Similar methods have already successfully monitored small-volume releases in past works (Bednar and Takahata 2021).

Thermally regulated multistage discharges from a pump were possible using selected successful (leak-free) pump chambers with an actuator. A final characterization of the release setup and the pump are provided in Sect. 3.6.

3.1 Actuator fabrication

A nitinol square, cut into a 25 mm x 25 mm section from a 200 micron thick sheet, was cleaned for copper deposition. The evaporation of 300 nm of copper onto the nitinol created a backing for the through etch. After the copper evaporation, Kapton tape served as an etch mask for the nitinol. Three layers of Riston Fx 930 resist, wet-laminated onto the tape using DI water and roller temperatures of 110 °C for the top and bottom with a feed speed of ~ 1 ft/min, served as pattern-cutting guides. Exposure through masks printed on mylar created the actuator patterns. The pattern contained an array of rectangles starting at 500 by 2,000 microns and increasing to 980 by 2,880 microns. The development was done in sodium carbonate in water for ~ 15 min. A rinse,

done under running tap water and then DI water, completed the development of the cutting guides. After drying the sample, another exposure improved resist adhesion. Cutting the Kapton tape under the patterned resist with a razor was done under a microscope. Using precision tweezers to pull off sections exposed the nitinol to be etched. Finally, the sample was covered with protective plastic and run back under the laminator to help with the adhesion of the Kapton tape.
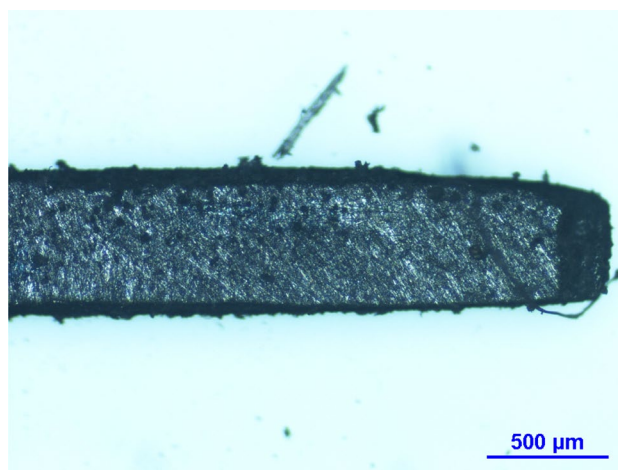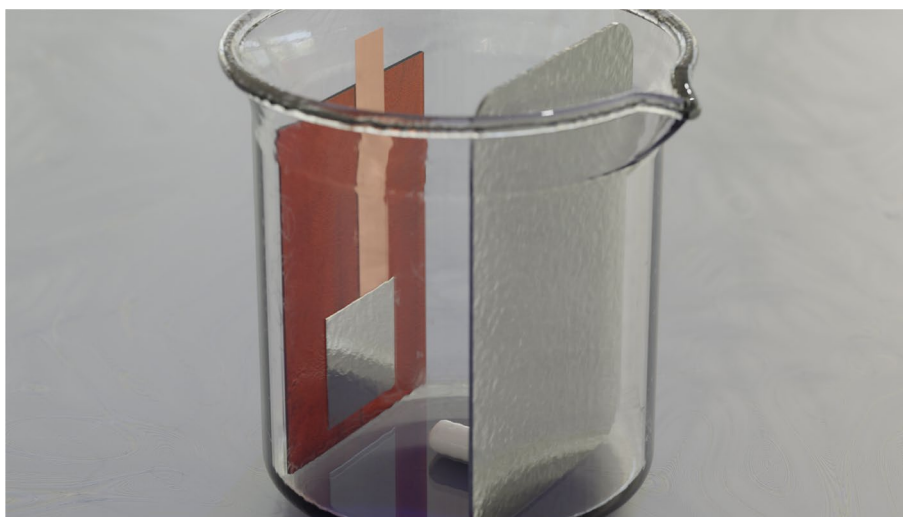
As preparation of an electrochemical etchant, ~ 2.1 g of lithium chloride was mixed with ~ 100 mL of ethanol, forming a 0.5 M solution. The solution was placed on a stirring plate until dissolved and left covered overnight. The patterned nitinol sample had its copper backing against the copper tape on the glass slides, as seen in the setup illustrated in Fig. 11.

The setup in the etchant solution used a small stirrer running on the lowest possible setting and applied 8 V between the anode (nitinol) and cathode (stainless steel plate). The current was ~ 40 mA to start. The process produced a highly directional etch. Then, the sample was cleaned of the copper using a ferric chloride etchant. Finally, removing the Kapton tape and mechanical polishing finished the nitinol actuator fabrication process. A microscope image of a completed actuator is shown in Fig. 12.

3.2 Pump chamber fabrication

Using microscope slides and a scoring pen, glass substrates of approximately 25 mm x 25 mm x 1 mm were prepared. The substrates were cleaned by rinsing with acetone, 2-propanol (IPA), and DI water. Once dried, three layers of negative photoresist (Riston FX930, DuPont, DE, USA) were wet laminated using DI water and roller temperatures of 110 °C for the top and bottom with a feed speed of ~ 1 ft/min (a total of 90 microns for the first layer seen in Fig. 13a). The through port and chamber patterns, shown in Fig. 13b,

Fig. 12 A microscope image of a nitinol actuator

were made with a maskless lithography system (MLA-150, Heidelberg Instruments, BW, DE). The development was done in sodium carbonate in water for ~ 12 min. A post-development rinse was done under running tap water and then rinsed with DI water. That created a negative space for the top of the device, seen in Fig. 13c. To smooth the edges and promote liftoff, ~ 10 µm of positive photoresist (AZ P4620, Merck KGaA, HE, DE) was spun onto the developed negative photoresist, pictured in Fig. 13d. The positive photoresist was hardbaked at 110 °C for 5 min.

The top device layer of the pump, visible in Fig. 13e, was made of parylene C. This was deposited by vapor deposition (PDS 2010, Specialty Coating Systems, IN, USA). The inside of the chamber and ports were filled with positive photoresist (AZ P4620). The surface was then knifed off, as represented by Fig. 13f, and the positive photoresist was hardbaked at 110 °C for 5 min. The inside of the channels connecting the ports to the chamber were patterned from
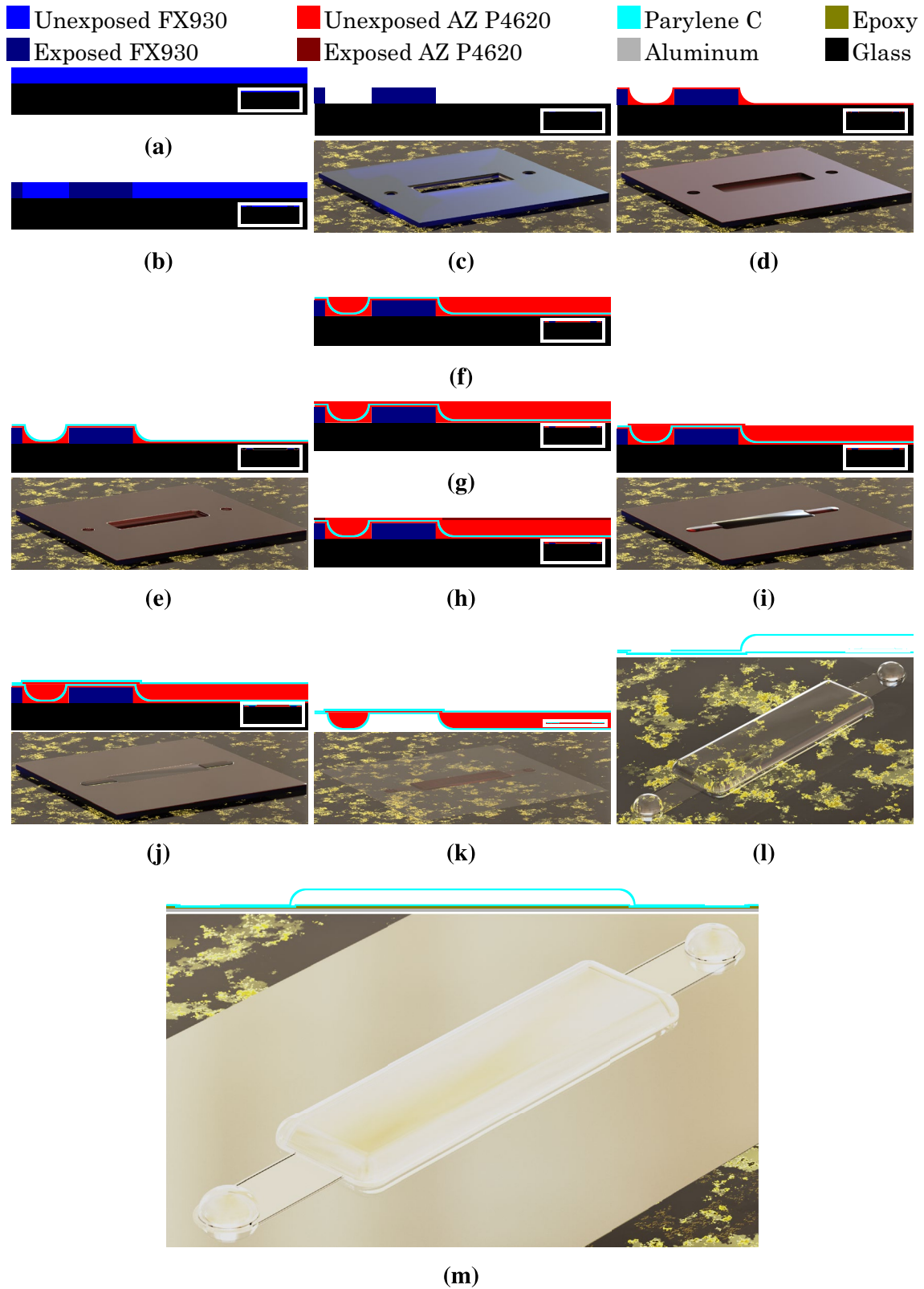
Fig. 11 A 3D computer-generated image of the electrochemical etch setup for nitinol etching. Inside the beaker is a stainless steel plate for the cathode, a magnet for stirring, and the nitinol holder. The nitinol holder is composed of a copper tape strip to connect to the anode side. The copper is taped to two taped-together microscope slides. The nitinol is held down against the copper tape with patterned Kapton tape (not shown to improve the clarity of the setup)

Fig. 13 A step-by-step, to-scale, side-view of the pump fabrication layers and 3D computer-rendered images of select pump fabrication steps created to-scale. To improve visibility of each layer, the side-view fabrication steps seen in **a–l** are cropped 75% vertically (cut from the bottom) and 50% horizontally (cut from the right) with insets of the full image

~ 10 µm of positive photoresist (AZ P4620) that was spun onto the hardbaked positive photoresist. This positive photoresist, illustrated in Fig. 13g, was softbaked at 110 °C for 90 s.

The channel patterns were exposed, as seen in Fig. 13h, using a maskless lithography system. Then, the patterned photoresist was developed for 7 min in a potassium based buffered developer (AZ 400K, Merck KGaA, HE, DE) diluted at a 1:4 ratio with DI water. At this point, all sacrificial fill components of the pump were complete, as depicted in Fig. 13i.

The bottom device layer was also made of parylene C. To promote adhesion between the two layers of parylene, the top layer along with the filled chamber and pattered channels were all placed in an oxygen plasma environment to clean and roughen the surface (Phantom RIE, Trion Technology, Inc., AZ, USA). Then, an adhesion promoter (3-(Trimethoxysilyl)propyl Methacrylate (stabilized with Butylated hydroxytoluene), TCI America, Ltd, OR, USA) was vapor deposited using a vacuum desiccator. Then, the bottom layer was vapor deposited, as indicated by Fig. 13j. A microscope image shows the fabrication layers up to this point in Fig. 14a.

Cutting along the edge of the substrate with a razor and immersing the device in acetone allowed the device to lift-off from the negative photoresist, as portrayed in Fig. 13k. As seen in Fig. 14b, the parylene cleanly lifts off from the mold created by the negative resist due to the thin positive resist liftoff layer. Then, cutting the ports with a razor and submerging the pump in acetone removed the sacrificial fill layers of positive photoresist, leaving only the parylene C shell, as depicted in Fig. 13l. This shell was then bonded, under slight pressure, bottom side (channel side) down to

aluminum foil using a resin epoxy. This bonding step, illustrated in Fig. 13m, created a closed chamber shell with normally closed channels acting as the inlet and outlet ports.

3.3 Actuator characterization

Confirming the possibility of piecewise actuation using a nitinol actuator was tested by mounting a prestressed actuator to a glass slide (Fig. 1). Bonding of the actuator was done using silver epoxy (CW2400, Chemtronics, GA, USA) to ensure solid adhesion and good thermal transfer. That glass slide was mounted to a Peltier heater (CP60301540, CUI Devices, OR, USA), and the stack containing the Peltier heater, glass slide, and nitinol actuator was all taped on top of a Peltier cooler (TEC1-12710, HB Electronic Components, SH, CN). A laser displacement sensor (LK-G32, Keyence, IL, USA) measured the distance from the actuator to the laser. Heating pulses performed with the Peltier heater allowed piecewise actuation.

The Peltier heater was wired to a power supply with the voltage limit set to 4.2 V, and the current limit was used to turn the device on and off. Increasing the on-time of the heater increased the maximum temperature reached. The SMM recovered back toward the glass it was mounted on until the actuator collided with the glass. To maintain the cooling of the experimental area, and avoid temperature run-off from the heating cycles of the Peltier heater, the whole experimental setup was placed onto the cooling side of the Peltier cooler. That cooler was attached with thermal paste (MX-4, Artic GmbH, NI, DE) to a water cooling block with water cycled through it with a temperature-controlled water pump. The temperature within the temperature-controlled water pump was chilled to 25 °C. This setup maintained a

(a)   **(b)**
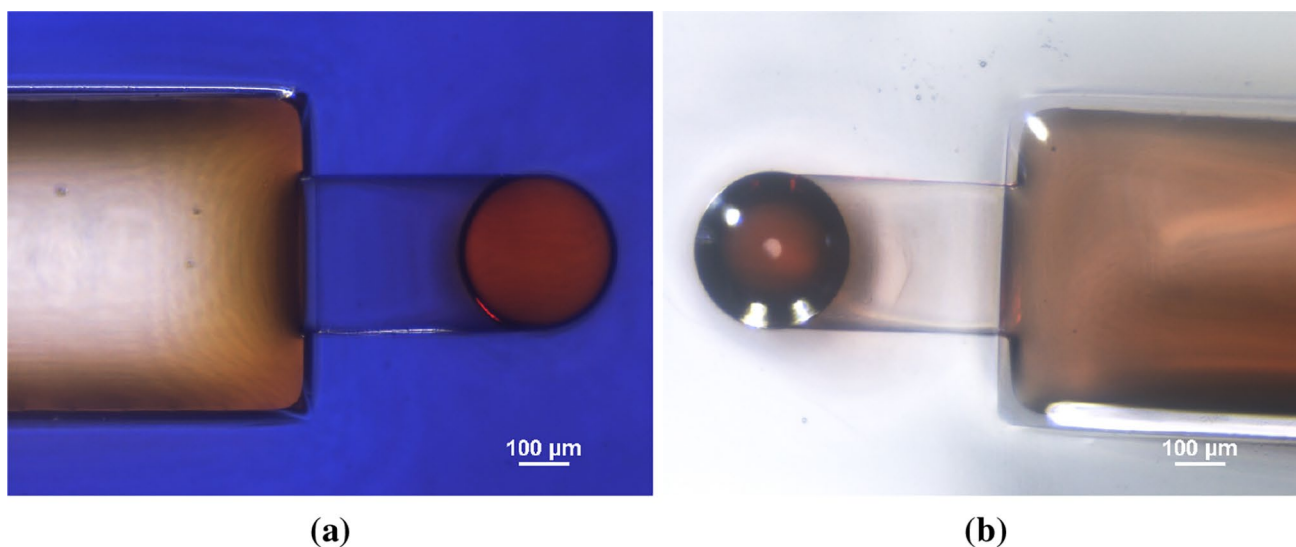
Fig. 14 Microscope images of the pump chamber, channel, and port showing **a** all deposited layers and **b** post stripping from the substrate

temperature of around 20 °C for the cooler by applying 1 A across the cooler with a power supply.

The fiber-optic temperature sensors and their software (detailed in Sect. 2.3) allowed for temperature data collection through the computer. The measurements from the laser and the temperature sensors were synchronized by post-alignment of data using signal interruptions from the laser caused at 10-s intervals according to the temperature sensor's timer. The laser connected to the computer via its controller (LK-G3001, Keyence, IL, USA) and data logging was managed by the supplied software (LK Navigator, Keyence, IL, USA).

3.4 Pump chamber characterization

Red food coloring in water added contrast to inspect for leaks, ensuring adhesion between parylene layers and effectiveness of the normally closed channels. As seen in Fig. 15a and 15b, this test was used before and after bonding to quickly filter out failed processes. There were multiple visual indicators for leaky devises. Prior to bonding, a drop of food-colored water left over a port would fill the chamber over a short time (Fig. 15a was taken during one of these moments), and leaks could be seen when fluid would flow outside the chamber boundaries, indicating poor sealing between parylene C layers.

Post-bonding, the channels acted as normally closed valves, requiring fluid pressure in order to fill the chamber. Thus, filling was achieved using a syringe and needle. When possible, a 32-gauge needle fit the port for filling the chamber; however, these would frequently clog, bend, or lose contact with the port, resulting in difficulties during filling. Thus, a 25-gauge needle was cut and filed flat at an angle to allow good contact over the port, which made an alternative for chamber filling.

If the chamber is no longer filled with red food-colored water after soaking in DI water, it was for an indication of outward flow leaks. The reverse test for inward flow was done by filling the chamber with water and soaking it in food-colored water. As exhibited by Fig. 15c, the normally-closed channels successfully kept out the food-colored water after a 24-hour soak.

3.5 Temperature-controlled release

Once again, the data collection setup described in Sect. 2.3 was utilized for collecting conductivity and temperature data during a temperature-controlled release from the pump. Inside a centrifuge tube was a magnetic stirrer separated into the conical section of the centrifuge tube by a perforated plate. The experimental area used 15 mL of DI water in the centrifuge tube.

The experimental area contained the pump, a heater, a conductivity probe, and two fiber-optic temperature sensors. One temperature sensor was near the conductivity sensor, held by its electrode support. The other sensor was taped to a glass slide mounted onto the heating side of the Peltier heater. On the glass was the actuator and pump chamber. The actuator, as described in Sect. 3.1, was mounted to the glass in the same manner as mentioned in Sect. 3.3 for actuator testing. It could then be reshaped from the prestressed curve to ~ 150 micron gap parallel with the glass slide. The pump chamber, fabricated as described in Sect. 3.2, was secured with scotch tape under the actuator. This resulted in a pump on top of the glass similar to that seen in Fig. 9. Taping allowed easy removal for refills between experiments as well as flexibility. Flexibility was tested by placing various slices of silicone lumps under the chamber–it was still operational with these varying surfaces underneath.

The Peltier heating device was powered as described in Sect. 3.3 during the piecewise actuation characterization. To maintain the cooling of the experimental area, and avoid temperature runoff from the heating cycles of the Peltier device, the whole experimental setup was placed
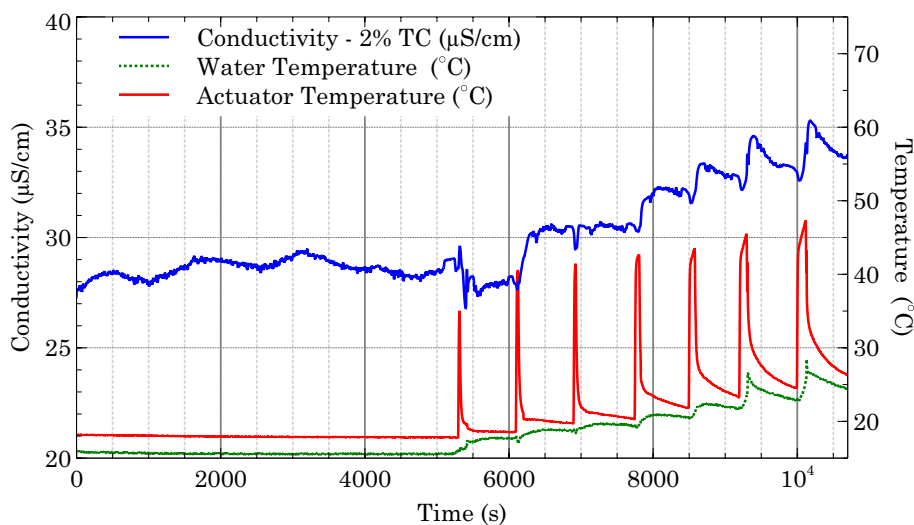

(a) **(b)** **(c)**
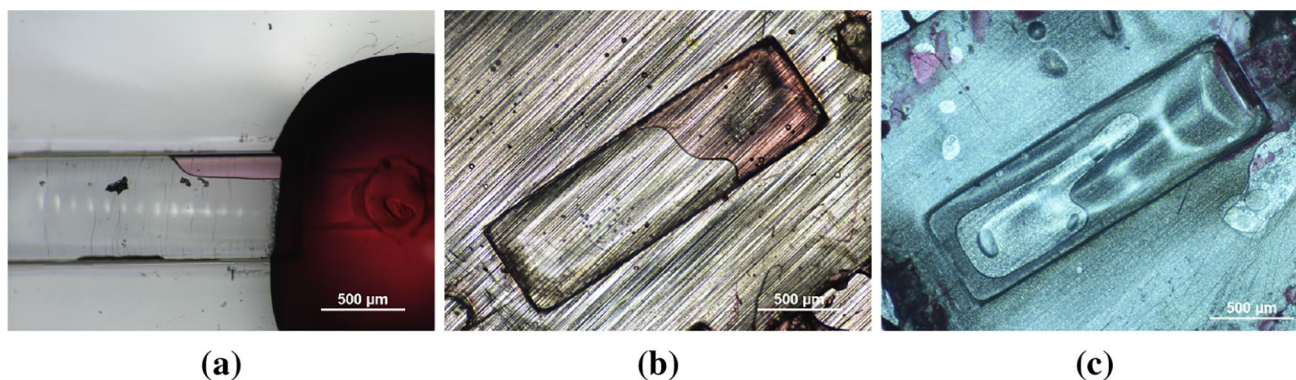
Fig. 15 Microscope images of two different pump chambers partially filled with red food-colored water **a** before bonding and **b** post bonding to aluminum foil and **c** a water-filled pump chamber after leak testing via 24 h of soaking in red food-colored water (color figure online)

into a cooling bath. This cooling bath was a beaker with water placed on top of the cooling side of the Peltier cooler setup as described in Sect. 3.3 for use during the actuator characterization. This setup maintained a temperature of around 7 °C for the cooling bath by applying 12 V across the cooler with a power supply.

3.6 Pump characterization

An explanation for temperature compensation and instrumental noise interference was presented in Sect. 2.4. A final control test was paramount in confirming that conductivity rises are attributable to releases from the pump. Therefore, a device was filled with saturated lithium chloride water and rinsed. Afterward, placement into the experimental setup accounted for all possibilities like oxidation or leaking from the device. Aside from leaking, oxidation from the aluminum foil, nitinol, or other metal components might release into the experimental area. Via this control test, all other elements within the experimental area were also checked. The same setup used in Sect. 3.5 was utilized for collecting conductivity and temperature data during the test. As seen in Fig. 16, after 5000 s of stirred immersion in water, conductivity measurements remained stable. Constant conductivity readings are a clear indication that the device was not leaking. A short series of temperature-controlled releases afterward indicated that the device was still functional (performed using the setup described in Sect. 3.5). Thus, no significant contributions to a change in the conductivity throughout the experiment should be from anything besides releases of lithium chloride water from the pump.

4 Results and discussion

The characterization of the nitinol actuator provided data for fitting the temperature to the shape recovery in Sect. 4.1. By using this as a model, it was possible to calculate the expected amount of release from the pump based on the temperature. This was done in comparison with actual release data in Sect. 4.2.

4.1 Piecewise actuator actuation and analysis

As described in Sect. 3.3, the piecewise actuation of the nitinol actuator was achieved by using increased heating times from the Peltier device. The initial location of the actuator, in comparison to its final position when hitting the glass, was used as a difference to calculate a percentage change toward complete contact with the glass slide. This percent displacement, along with the actuator temperature and cooler temperature, is shown in Fig. 17. After the first three pulses, the time between pulses was determined by actuator temperature. After each heating pulse enough time was given for the actuator to cool down below 25 °C. This was to allow a set reference temperature in showing the increasing level of actuation after each pulse. As seen in Fig. 17, the shape recovery moved the actuator closer to the glass slide at each pulse from the first to the tenth pulse. This is a logical and expected result as the actuator is hitting the glass slide by the tenth pulse. The total displacement from start to finish was measured as 1.4617 mm. The starting distance from the laser was calculated from averaging 22 values prior to the first pulse, and the final distance was calculated from averaging 172 values from when the actuator was in contact with the glass slide during the last pulse.

Fig. 16 A graph showing conductivity data, water temperature, and actuator temperature measured in 15 mL of water in a centrifuge tube. All elements used in a pump release experiment are within the centrifuge tube. A short series of releases are conducted after 5000 s, confirming that the device is functional

Fig. 17 A graphical illustration of the percent displacement of the actuator along with the simultaneous recording of the Peltier cooler temperature and the actuator's temperature (as measured from the surface of the glass)
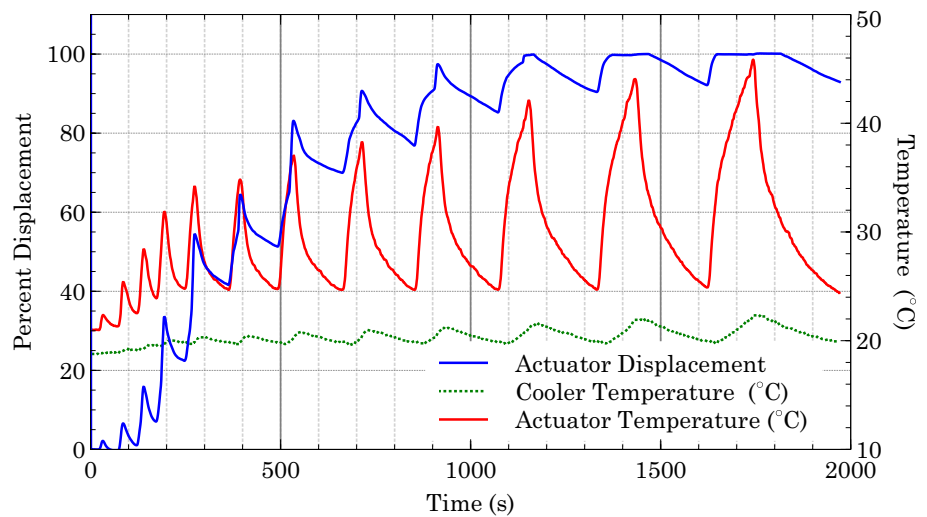
To further support the nitinol actuation as the cause of each release, the actuator displacement, from Fig. 17, was fit to a logistic curve (Eq. 3).

$$\frac{U}{1 + e^{-k(T-T_0)}} + L \tag{3}$$

Using the maximum actuator temperature achieved during each heating pulse as the variable, T, this fitted logistic curve reasonably characterizes the temperature dependence of the actuation. As seen in Fig. 18, the last three data points were excluded from the fit as the actuator was already in contact with the glass for those points. The upper limit of the function ($U + L$) occurs as $T \to \infty$. Using a number higher than 100 allows this modeling of actuation to reach completion (100) at a physically meaningful value, the temperature where the transformation from martensite to austenite finishes. Similarly, a lower limit (L) above zero allows for matching to the temperature where this transformation

begins. The equation is offset (T_0) to center between these transformation values, and the rate at which the transformation occurs is matched using the slope of the function (k).

4.2 Temperature-controlled release and analysis

Every 1000 s, the DC power supply for the Peltier heater was turned on for 120 s. Notice in Fig. 19 that these pulses caused an actuation of the nitinol actuator that pressed down on the pump. The actuation caused a release of the lithium chloride water contained within. After the actuation ceased, so did the pumping of the device. Consequently, the conductivity would eventually stabilize as the release of the lithium chloride water would stop. Complete actuation of a SMM actuator is not instantaneous. Controlling the supplied power to a heating device for a specified period allows piecewise controlled actuation of the nitinol actuator. Thus, subdividing a single actuation down onto the pump chamber allows multiple controlled releases. This behavior was also

Fig. 18 A graph with an iteratively fit logistic function to the actuator displacement versus the corresponding maximum actuator temperature from data seen in Fig. 17
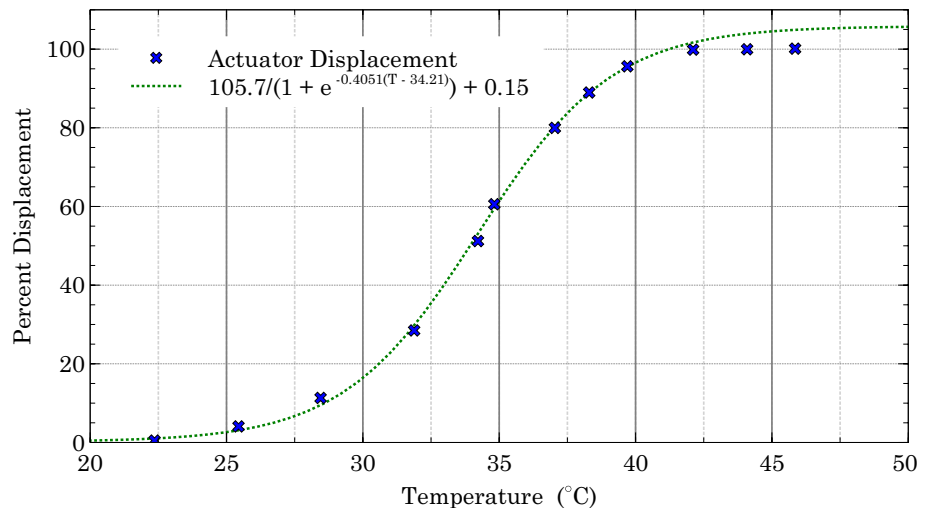
Fig. 19 A graphical representation of the experimental data collected during a temperature-controlled release experiment from a device constructed as shown in Fig. 9
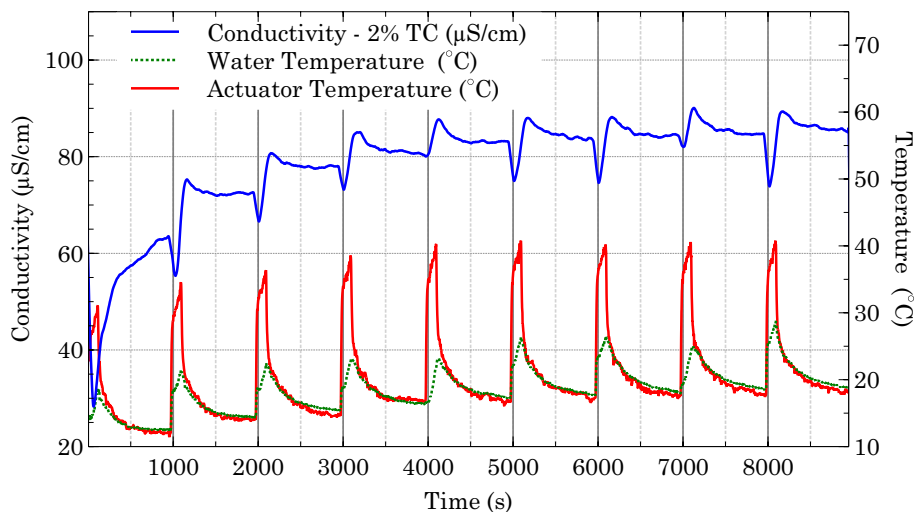
confirmed by the characterization of the actuator in Sect. 3.3 and illustrated in Fig. 17.

The maximum achieved actuator temperature from Fig. 19 was input into the fitted logistic function to calculate the amount of expected release based on the maximum achieved actuator temperature. This actuator temperature-dependent release amount was graphed alongside the measured release amount as calculated from the differences in the average conductivity values. As seen in Fig. 20, there is a good correlation between the conductivity-dependent release amount and the amount of expected release calculated from the maximum actuator temperature.

Since the theoretically expected percent release, based on the correlated maximum temperature achieved by the actuator as observed for each given release, falls within the uncertainty of the measured release, calculated using standard deviations from averaged conductivity data, these values are in good agreement. Thus, the fitting for the actuation was sufficient for predictive modeling, as confirmed by the experimental results. The correlation validates the intended functionality of the pump, and piecewise temperature-controlled release has been successfully demonstrated from a proof-of-principle device.
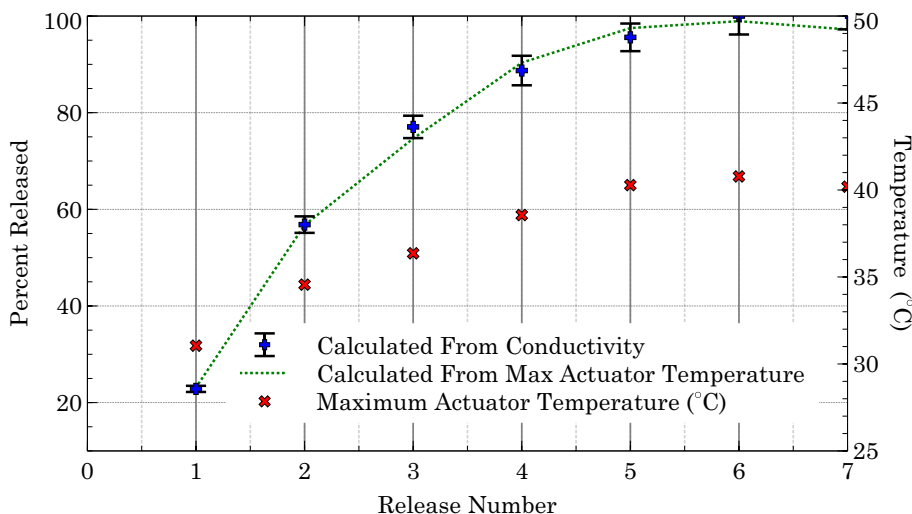
Fig. 20 Release amounts (percent) calculated from measured conductivity values are compared with theoretically expected release amounts. Each stable section from Fig. 19 was averaged for the conductivity value correlated to a release event. The average conductivity for the sixth release (the maximum temperature achieved in all the releases) and the base value was used as the total release difference to calculate the percent released. The theoretically calculated release values use the fit equation from Fig. 18 and the maximum temperature achieved by the actuator for each given release

5 Conclusion

Here, we have presented a proof-of-principle demonstration of multiple thermally controllable releases from a flexible parylene C micropump by utilizing a nitinol SMM actuator. Two findings validated in these works offer substantial insight: highly controllable piecewise actuation of SMMs and normally closed channels utilizing material elasticity for operation. Future experiments could determine the upper and lower limits of scaling this pump design. We expect an upper limit when an actuator large enough to evacuate an entire chamber would be more space wasteful than a typical reservoir and pump chamber design. Thus, a different mechanism for driving the fluid may be favorable for large pumps. On the lower limit, the normally closed flexible channels might no longer be large enough to allow passage driven by increasing pressure from the chamber. Both of these limits likely vary depending on the specifics of an application. Yet, having a generalized idea of where these limits lie is of paramount importance. This knowledge contributes toward determining the probability of successful implementation when considering potential uses for this pump design. For example, with the possibility of miniaturization, the high chemical compatibility of the chamber, and the biocompatibility of the materials involved in the device's construction, this pump will make a good candidate for in vivo drug delivery applications.

Author contributions VBB conceptualized and conducted the research, analyzed the data, prepared the figures, and wrote the manuscript. KT reviewed the manuscript.

Data availability All pertinent data used in the findings of this study are in this publication. Please send any reasonable requests for alternative data formats to the corresponding author.

Declarations

Conflict of interest The authors declare that they have no conflict of interest.

References

Abdullah EJ, Soriano J, de Bastida-Fernàndez Garrido I et al. (2021) Accurate position control of shape memory alloy actuation using displacement feedback and self-sensing system. Microsyst Technol 27(7):2553–2566. https://doi.org/10.1007/s00542-020-05085-0

Alaneme KK, Okotete EA (2016) Reconciling viability and cost-effective shape memory alloy options—a review of copper and iron based shape memory metallic systems. Eng Sci Technol Int J 19(3):1582–1592. https://doi.org/10.1016/j.jestch.2016.05.010 (www.sciencedirect.com/science/article/pii/S2215098616301070)

Babu B, Mathew R (2014) Experimental investigation on shape recovery force of shape memory alloy (nitinol) at various temperatures under constant strain. Int J Appl Eng Res 9:11353–11364

Barua R, Datta S, Sengupta P et al. (2021) Chapter 14—Advances in mems micropumps and their emerging drug delivery and biomedical applications. In: Nayak AK, Pal K, Banerjee I et al. (eds) Advances and challenges in pharmaceutical technology. Academic Press, pp 411–452. https://doi.org/10.1016/B978-0-12-820043-8.00002-5

Bednar VB, Takahata K (2021) A thermosensitive material coated resonant stent for drug delivery on demand. Biomed Microdevice 23:18. https://doi.org/10.1007/s10544-021-00548-1

Chappel E, Dumont-Fillon D (2021) Chapter 3—Micropumps for drug delivery. In: Chappel E (ed) Drug delivery devices and therapeutic systems. Developments in biomedical engineering and bioelectronics. Academic Press, pp 31–61. https://doi.org/10.1016/B978-0-12-819838-4.00015-8

Chen CL, Selvarasah S, Chao SH et al. (2007) An electrohydrodynamic micropump for on-chip fluid pumping on a flexible parylene substrate. In: 2007 2nd IEEE international conference on nano/micro engineered and molecular systems, pp 826–829. https://doi.org/10.1109/NEMS.2007.352145

Christov IC, Cognet V, Shidhore TC et al. (2018) Flow rate-pressure drop relation for deformable shallow microfluidic channels. J Fluid Mech 841:267–286. https://doi.org/10.1017/jfm.2018.30

Cohen-Adad R (1991) Lithium chloride. In: Cohen-Adad R, Lorimer JW (eds) Alkali metal and ammonium chlorides in water and heavy water (binary systems). IUPAC solubility data series. Pergamon, Amsterdam, pp 1–63. https://doi.org/10.1016/B978-0-08-023918-7.50007-7

Cohen-Adad R, Vallée P, Lorimer J (1991) Potassium chloride. In: Cohen-Adad R, Lorimer JW (eds) Alkali metal and ammonium chlorides in water and heavy water (binary systems). IUPAC solubility data series. Pergamon, Amsterdam, pp 210–343. https://doi.org/10.1016/B978-0-08-023918-7.50009-0

Emerson Process Management (2010) Conductance data for commonly used chemicals. Emerson Electric Co., https://www.emerson.com/documents/automation/manual-conductance-data-for-commonly-used-chemicals-rosemount-en-68896.pdf

Fallahi H, Zhang J, Phan HP et al. (2019) Flexible microfluidics: fundamentals, recent developments, and applications. Micromachines 10(12):830. https://doi.org/10.3390/mi10120830

Forouzandeh F, Arevalo A, Alfadhel A et al. (2021) A review of peristaltic micropumps. Sens Actuators A 326:112602. https://doi.org/10.1016/j.sna.2021.112602

Kumar P, Lagoudas D (2008) Introduction to shape memory alloys. Springer US, Boston, pp 1–51. https://doi.org/10.1007/978-0-387-47685-8_1

Lee YS, Bhattacharjee N, Folch A (2018) 3d-printed quake-style micro-valves and micropumps. Lab Chip 18:1207–1214. https://doi.org/10.1039/C8LC00001H

Mehboudi A, Yeom J (2019) Experimental and theoretical investigation of a low-Reynolds-number flow through deformable shallow microchannels with ultra-low height-to-width aspect ratios. Microfluid Nanofluid 23:66. https://doi.org/10.1007/s10404-019-2235-9

Miller DA, Lagoudas DC (2000) Thermomechanical characterization of NiTiCu and NiTi SMA actuators: influence of plastic strains.

Smart Mater Struct 9(5):640. https://doi.org/10.1088/0964-1726/9/5/308

Mineta T (2003) Electrochemical etching of a shape memory alloy using new electrolyte solutions. J Micromech Microeng 14(1):76. https://doi.org/10.1088/0960-1317/14/1/310

Mineta T, Makino E (2010) Characteristics of the electrochemical etching of TiNi shape memory alloy in a LiCl-ethanol solution. J Micromech Microeng 20(12):125012. https://doi.org/10.1088/0960-1317/20/12/125012

Mohith S, Karanth PN, Kulkarni S (2019) Recent trends in mechanical micropumps and their applications: a review. Mechatronics 60:34–55. https://doi.org/10.1016/j.mechatronics.2019.04.009

Mähler J, Persson I (2012) A study of the hydration of the alkali metal ions in aqueous solution. Inorg Chem 51(1):425–438. https://doi.org/10.1021/ic2018693. (**pMID: 22168370**)

Ni C, Chen D, Yin Y et al. (2023) Shape memory polymer with programmable recovery onset. Nature. https://doi.org/10.1038/s41586-023-06520-8

Ozdemir O, Karakashev SI, Nguyen AV et al. (2009) Adsorption and surface tension analysis of concentrated alkali halide brine solutions. Miner Eng 22(3):263–271. https://doi.org/10.1016/j.mineng.2008.08.001

Renata C, Huang WM, He LW et al. (2017) Shape change/memory actuators based on shape memory materials. J Mech Sci Technol 31(10):4863–4873. https://doi.org/10.1007/s12206-017-0934-2

Rumble JR (ed) (2023) Electrical conductivity of aqueous solutions at 20°C as a function of concentration, 104th edn. CRC Press/Taylor & Francis. https://hbcp-chemnetbase-com.eu1.proxy.openathens.net/documents/05_17/05_17_0001.xhtml?dswid=-6452

Song R, Zou T, Chen J et al. (2019) Study on the physical properties of LiCl solution. IOP Conf Ser Mater Sci Eng 562(1):012102. https://doi.org/10.1088/1757-899X/562/1/012102

Tang Z, Shao X, Huang J et al. (2020) Manipulate microfluid with an integrated butterfly valve for micropump application. Sens Actuators A 306:111965. https://doi.org/10.1016/j.sna.2020.111965

Wang YN, Fu LM (2018) Micropumps and biomedical applications—a review. Microelectron Eng 195:121–138. https://doi.org/10.1016/j.mee.2018.04.008

Wu X, Huang WM, Zhao Y et al. (2013) Mechanisms of the shape memory effect in polymeric materials. Polymers 5(4):1169–1202. https://doi.org/10.3390/polym5041169

Yamashita K, Shimamoto A (2005) Control of shape recovery force in SMA fiber reinforced composite materials. In: Armstrong WD (ed) Smart structures and materials 2005: active materials: behavior and mechanics. International Society for Optics and Photonics, vol 5761. SPIE, pp 429–439. https://doi.org/10.1117/12.599381